Highly-Stable Organo-Lead Halide Perovskites Synthesized Through Green Self-Assembly Process

Congcong Wu, Haijin Li, Yongke Yan, Bo Chi, Kristen M. Felice, Robert B. Moore, Brenden A. Magill, Rathsara R. H. H. Mudiyanselage, Giti A. Khodaparast, Mohan Sanghadasa, and Shashank Priya**

Although unprecedented conversion efficiency has been achieved in organic–inorganic hybrid perovskite solar cells (PSCs), their long-term stability has remained a major issue in their transition. Here, we demonstrate a highly-stable $CH_3NH_3PbI_3$ ($MAPbI_3$) perovskite using a green self-assembly (SA) process that provides a major breakthrough in resolving this issue. In this process, the hydrophobic polymer, poly(methyl methacrylate) (PMMA), is introduced into the 2D layered $MAPbI_3$ perovskite intermediates, resulting in chemical coordination and self-assembly into 3D perovskite grains with PMMA coated along the grain boundaries. The bilayer grain boundary effectively blocks moisture corrosion thereby significantly improving the stability of $MAPbI_3$ perovskite. Further, PMMA is found to reduce the trap density by electronically compensating the iodide vacancy along the boundary, which decreases the charge recombination and improves the open circuit voltage of PSCs. The PSCs comprising the $MAPbI_3$–PMMA layer show excellent stability under high moisture conditions, exhibiting no phase change under ≈70% humidity for over 31 days (approximately 500% higher compared to state-of-the-art) and excellent performance in 50–70% humidity for over 50 days.

Dr. C. Wu, Dr. Y. Yan, Prof. S. Priya
Center for Energy Harvesting Materials and System (CEHMS)
Virginia Tech
Blacksburg, VA 24061, USA
E-mail: ccw39@vt.edu; spriya@vt.edu

H. Li, Prof. B. Chi
Center for Fuel Cell Innovation
School of Materials Science and Engineering
Huazhong University of Science &Technology
Wuhan 430074, China

K. Felice, Prof. R. Moore
Department of Chemistry and Macromolecules Innovation Institute
Virginia Tech
Blacksburg, VA 24061, USA

Dr. B. Magill, R. Mudiyanselage, Prof. G. Khodaparast
Department of Physics
Virginia Tech
Blacksburg, VA 24061, USA

Dr. M. Sanghadasa
Aviation and Missile Research, Development, and Engineering Center
US Army RDECOM
Redstone Arsenal, AL 35898, USA

DOI: 10.1002/solr.201800052

Organic–inorganic hybrid perovskite solar cells (PSCs) have attracted tremendous attention in past few years, owing to the unprecedented enhancement in light-electricity conversion efficiency[1–4] and progress made in their facile cost-effective fabrication.[5–7] The unique characteristics of PSCs including high extinction coefficient[8] and long charge carrier diffusion length[9] distinguish them from other types of solar cells. However, the low long-term stability is regarded as the most critical challenge in implementation of PSCs. The perovskite layer is sensitive to humidity, oxygen, thermal, and ultra-violet (UV) radiation. These external stimuli can cause the irreversible decomposition of the perovskite light absorber and thus deteriorate the performance permanently. In order to enable the transition of PSCs, the stability issue has to be resolved. Further, the fabrication process for PSCs needs to be developed in an environmentally friendly way.[10] Here, we provide breakthrough on both these fronts, demonstrating an ultra-high stability PSC using green fabrication process.

Solar cell encapsulation with a polymer sealant has been shown to prolong solar cell lifetime by blocking water and oxygen from penetrating the perovskite layer.[11,12] Bella et al. demonstrated a photocurable fluoropolymer outer cover layer that formed a strongly hydrophobic moisture barrier. Using this barrier layer, the lifetime of the encapsulated device was extended by 6 months.[13] Physical encapsulation is an effective protection for the device, but it is not permanent solution for addressing the intrinsic instability of perovskites. Another approach for improving the long-term stability is to deposit a hydrophobic capping layer on top of perovskite light absorber. Bai et al. used silane-functionalized fullerene as the top electron transport layer where the cross-linked hydrophobic silane repelled the water and improved the stability against moisture.[14] Although the hydrophobic capping layer on top can hinder the moisture degradation along the out-of-plane direction, the degradation can still occur along in-plane direction.[15] Additionally, the thickness of the capping layer must be accurately controlled to enable both moisture blocking and charge carrier transfer.

The incorporation of polymer materials is an effective method for the stabilization of solar cells, which have been utilized in organic photovoltaics (OPV) and dye sensitized solar cells (DSSCs).[16–19] The polymer materials have been employed to replace the organic solvent in the electrolyte of DSSCs, avoiding the evaporation and leakage of the liquid electrolyte. The stability of the gel or solid-state DSSCs could be largely improved by the introduction of the polymer matrix. In terms of moisture barrier for perovskite, the polymer PMMA has superior hydrophobicity and the lone pair electrons on carbonyl oxygen could serve as the interaction site. The utilization of polymer in perovskite solar cell has been reported previously, however, mostly as the capping layer on top of perovskite.[20,21] In comparison to the outer protective layer, the perovskite grain with a molecular-level protection inside the thin film would be more promising for the stability improvement.

Here, we report a novel synthesis process for the perovskite thin film by exfoliating and self-assembling the perovskite single crystals. This process is found to provide a highly stable and low trap-state density film. The $MAPbI_3$ single crystal was exfoliated by methylamine CH_3NH_2 and then transformed into liquid 2D layered perovskite intermediates (LPI). The exposed cations in the basal plane provide active sites for the complexation between LPI and PMMA, and the sequential self-assembly (SA) of the complexed LPI results in the perovskite grains coated with a monolayer of PMMA protective layer, providing a homogeneous hybrid microstructure where encapsulation occurs at the molecular level. The perovskite light absorber not only provides high stability against moisture, oxygen and light, but also passivates the trap densities along the perovskite grain boundary, thereby effectively reducing interfacial charge carrier recombination. The complexation of PMMA with perovskite grains offers full protection against the environmental factors while providing high photovoltaic performance. In comparison to the conventional perovskite layer, which decomposes within 6 days under 70% relative humidity, the $MAPbI_3$–PMMA perovskite synthesized via the SA process endures up to 31 days without any phase change (ca. 500% improvement) and demonstrates a promising solar cell performance under 50–70% humidity over 50 days. This success provides fundamental breakthrough required toward realizing stable PSCs without sacrificing photovoltaic performance.

Self-Assembly Process: **Figure 1** describes the fabrication of boundary coated perovskite thin film through the self-assembly process. $MAPbI_3$ perovskite single crystal has been shown to possess well-ordered lattice structure and negligible internal defects. This imparts long charge carrier diffusion length[22] and low trap-state density.[23] If the perovskite thin film could be directly synthesized from single crystals, it would be expected to possess these superior properties for thin film. The 3D perovskite material has ABX_3 crystal structure, where A site is organic or inorganic cation, B is typically metal cation, and X is the halide. Excess A site cations can be introduced in ABX_3 perovskite which results in transformation of the 3D framework into 2D layered structure due to the confinement of the inorganic framework.[24] As shown in Figure 1a and b, upon the exposure of $CH_3NH_3PbI_3$ single crystal to methylamine CH_3NH_2 gas, the black single crystal is converted into clear yellow liquid. This is attributed to the continuous intercalation of CH_3NH_2 into 3D structure, resulting in the collapse of 3D frameworks and formation of 2D layered perovskite intermediates (LPI).[25] Movie S1, Supporting Information shows the transition of the LPI solution during spin-coating. After the evaporation of the solvent and CH_3NH_2, the LPI self-assembles into 3D black perovskite

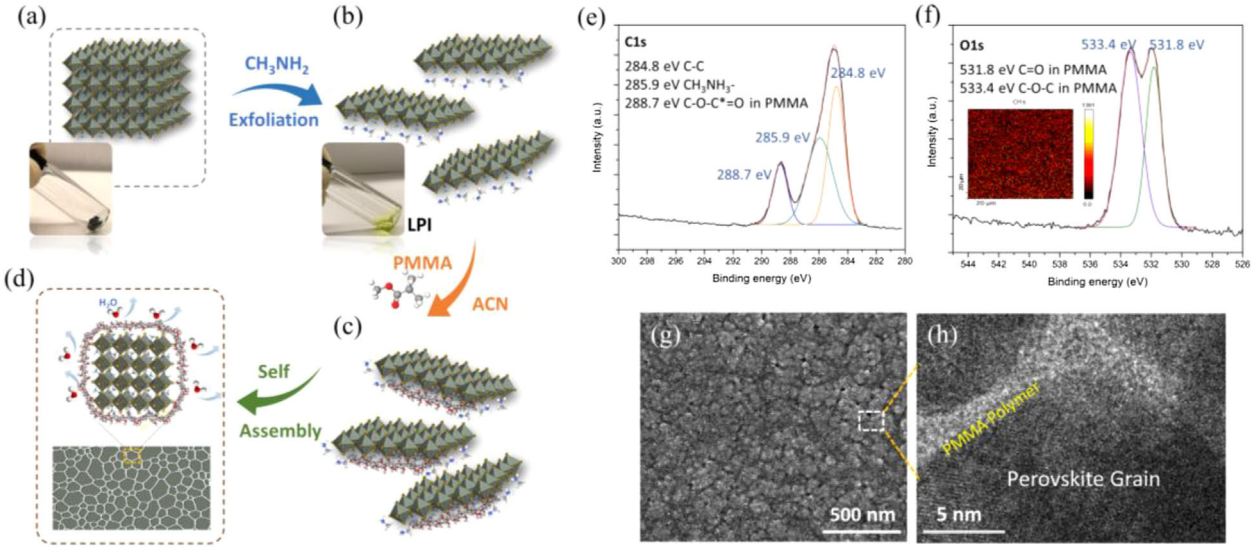

Figure 1. The fabrication of boundary coated perovskites through the self-assembly process. a) The single crystal of $MAPbI_3$ perovskite. b) The formation of 2D layered perovskite intermediates (LPI). The $MAPbI_3$ single crystal is exfoliated using CH_3NH_2. During this step, the solid crystal turns into clear yellow liquid. c) The complexation between LPI and PMMA chain. d) The self-assembly of LPI and PMMA complexation. Upon evaporation of solvent and CH_3NH_2, the layered perovskite is self-assembled, leaving PMMA anchored at the boundary of perovskite grains. e) XPS of $MAPbI_3$–PMMA film in C1s region. f) XPS of $MAPbI_3$–PMMA film in O1s region, where the image of O1s mapping has been inserted. g) SEM of $MAPbI_3$–PMMA film. h) HRTEM cross-section image of $MAPbI_3$–PMMA film, where the amorphous PMMA is detected at the boundary of perovskite grains.

immediately without any post-treatment. Since the LPI has a number of active sites, it is feasible to modify the LPI by introducing the hydrophobic polymer PMMA, and the sequential self-assembly process could result in a homogenous hybrid film. Due to the O—H bonding between the carbonyl oxygen in PMMA and $CH_3NH_3^+$, the PMMA polymer chain is anchored to the LPI, as illustrated in Figure 1c. After the evaporation of solvent and CH_3NH_2, the complexed LPI tends to self-assemble into 3D perovskite, and the anchored PMMA polymer chain locates itself at the boundary of the newly formed perovskite grains. This results in a uniform hybrid film where perovskite grains are coated with a monolayer of PMMA polymer chain, as elucidated in Figure 1d. The hydrophobic polymer essentially protects the perovskite grains from degradation by moisture and oxygen.

X-ray photoelectron spectroscopy (XPS) was performed to analyze the chemical composition of the perovskite film synthesized through the self-assembly of LPI and PMMA complexation ($MAPbI_3$—PMMA), as shown in Figure 1e and f. In the C1s region, there are three peaks located at 284.8, 285.9, and 288.7 eV, respectively. The peak at 284.8 eV is ascribed to the component of C—C, mainly from the PMMA polymer chains. The peak at 285.9 eV belongs to $CH_3NH_3^+$ in perovskite, and the peak located at 288.7 eV is a characteristic of ester (O—C*=O) in PMMA, as shown in Figure 1e. In the O1s region, we observe two peaks located at 531.8 and 533.4 eV, which are the typical features of C=O and C—O—C in PMMA. The image of XPS mapping ($300 \times 300\ \mu m^2$ area) of the O1s is inserted in Figure 1f, revealing the uniformly distributed PMMA in the perovskite film. Figure 1g displays the scanning electron microscopy (SEM) image of the $MAPbI_3$—PMMA film. Unlike the $MAPbI_3$ film without PMMA (Figure S1, Supporting Information), the $MAPbI_3$—PMMA film is comprised of small perovskite grains with sizes ranging from 100–200 nm, which is probably due to the anchored PMMA polymer chains on the LPI that impedes the grain growth during the SA process. Figure 1h shows the high-resolution transmission electron microscopy (HRTEM) cross-sectional image of the $MAPbI_3$–PMMA film. It can be observed in this image that an amorphous region with thickness of 2–3 nm is present at grain boundary. This confirms that the amorphous PMMA polymer forms a protective layer over the perovskite grain boundary via the SA process. The conductive atomic force microscopy (c–AFM) analysis of the $MAPbI_3$—PMMA film is shown in Figure S2, Supporting Information. The perovskite grain boundary shows darker contrast compared with that inside the perovskite grain, further suggesting that the hydrophobic polymer PMMA is principally located at the grain boundary.

Stability Improvement: To test the moisture stability of the perovskite layers, we measured and compared the X-ray diffraction (XRD) patterns of three types of perovskite films which were stored at 70% relative humidity for 31 days. The precursor—$MAPbI_3$ denotes the perovskite film synthesized from GBL/DMSO perovskite precursor solution via anti-solvent method. LPI—$MAPbI_3$ and $MAPbI_3$—PMMA describe the perovskite film synthesized through self-assembly of the LPI without and with PMMA complexation, respectively. The chemical reaction of $MAPbI_3$ perovskite with water causes the decomposition of perovskite into PbI_2, therefore, we use the relative amount of formed PbI_2 to evaluate the stability against moisture corrosion. **Figure 2**a shows the XRD peak intensity ratio of PbI_2 (001 plane, 12.7°) to that of $MAPbI_3$ (110 plane, 14.1°) as a function of aging time. Corresponding XRD patterns of the three films during the 31 days period are presented in Figure S3, Supporting Information. The precursor—$MAPbI_3$ film rapidly decomposed to PbI_2 in just few days (less than 6 days), while the LPI—$MAPbI_3$ film shows better stability but began to decompose before day 9. The $MAPbI_3$—PMMA film shows a significantly improved moisture stability, and a minor PbI_2 peak emerged after day 21. The peak intensity ratio of the precursor—$MAPbI_3$ film increases sharply and reaches a maximum of 28.07 on the 31st day, which indicates nearly complete conversion to PbI_2. In contrast, the LPI—$MAPbI_3$ perovskite film exhibits a much slower degradation rate, with a maximum peak ratio of 4.36 on day 31. For the $MAPbI_3$—PMMA film, the peak ratio is almost unchanged throughout the experiment and the film remains entirely black. As expected, the perovskite film synthesized from precursor solution is sensitive to moisture exposure, exhibiting a rapid decomposition rate. The stability improvement for the $MAPbI_3$ film by LPI is ascribed to the self-assembly process, which probably leads to enhanced grain boundary strength. The modification of LPI by PMMA complexation leads to a further improved moisture stability through the self-assembled hydrophobic PMMA coating over the perovskite grain boundary, exhibiting almost no crystal structure change over 31 days under high humidity exposure.

In addition to moisture, light and oxygen (O_2) can also trigger and accelerate the irreversible degradation of $MAPbI_3$ perovskites.[26,27] Figure 2b demonstrates the XRD of the three perovskite films after 5 h of exposure under one sun illumination (AM 1.5) in ambient air (ca. 50% relative humidity). The precursor—$MAPbI_3$ film entirely converted to PbI_2, as evidenced by the peak at 12.7° (PbI_2 001 plane). The LPI—$MAPbI_3$ film partially degraded to PbI_2, resulting in the same peak intensity for PbI_2 (001) and perovskite (110). In contrast, the $MAPbI_3$—PMMA film did not exhibit any degradation under the constant illumination. The perovskite degradation under illumination with oxygen in the environment is associated with the localized traps along the grain boundary, where trapped photo-excited electrons can react with oxygen to form superoxide O_2^-, and consequently the superoxide can activate the perovskite degradation to PbI_2.[28] Typically, vacancies along the boundary act as charge carrier traps that react with atmospheric oxygen. The I^- vacancy is the most energetically favorable site for oxygen reduction. In the case of $MAPbI_3$—PMMA perovskite, the C=O oxygen in PMMA serves as an electron donor, which can passivate the charge traps by occupying the I^- sites to compensate for the electronic loss at the grain boundary, illustrated in Figure 2c.

One thought that may come to mind is "how about directly dissolving the PMMA in the perovskite precursor solution?" In order to address this question, we compared the stability between the perovskite film synthesized from perovskite precursor solution with dissolved PMMA and $MAPbI_3$—PMMA through SA process by illuminating the films under 1 sun condition in ambient air for 2 h. It was found that the perovskite film fabricated from perovskite precursor solution with dissolved PMMA decomposed rapidly, with ca. A 90% area of the film

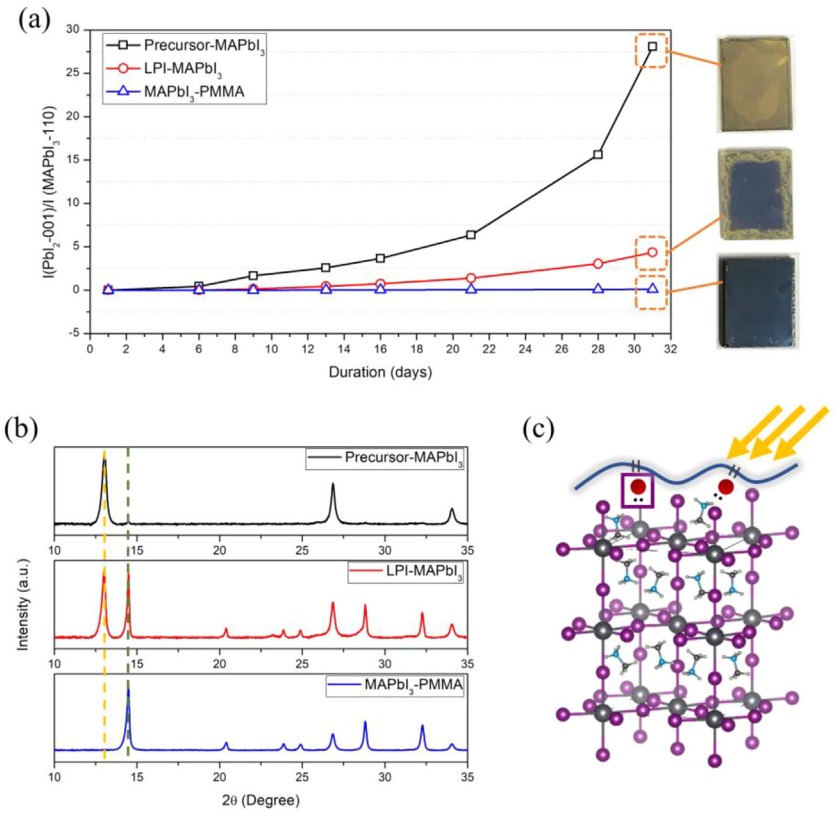

Figure 2. Stability of perovskite against moisture, light, and oxygen. a) XRD peak intensity ratio of PbI_2 (001 plane, 12.7°) to $MAPbI_3$ (110 plane, 14.1°) versus time for the precursor−$MAPbI_3$ film, LPI−$MAPbI_3$ film, and $MAPbI_3$−PMMA film. The XRD of the three perovskite films were measured during 31 days of 70% humid air exposure. b) XRD of precursor−$MAPbI_3$ film, LPI−$MAPbI_3$ film, and $MAPbI_3$−PMMA film after 1 sun illumination in ambient air (ca. 50% relative humidity) for 5 h. c) Schematic illustration of the electronic passivation of iodide vacancy defects by PMMA layer at the boundary of perovskite grain.

converted to PbI_2. In contrast, the $MAPbI_3$−PMMA film obtained through SA process did not show any degradation for a prolonged period (Figure S4a, Supporting Information). The SEM of the perovskite film fabricated by perovskite precursor solution with dissolved PMMA is shown in Figure S4b and c, Supporting Information. It shows a microstructure of randomly distributed dendrites comprising of small perovskite grains, which is probably due to the random distribution of PMMA polymer chain preventing the nucleation of perovskite grains. The results indicate that the process for incorporating PMMA in perovskite has a crucial impact on the microstructure and the corresponding properties. The remarkable stability of $MAPbI_3$−PMMA is ascribed to the self-assembly of the LPI and PMMA complexation, resulting in protection at molecular scale through modification of the grain boundary structure.

Photovoltaic Performance: **Figure 3**a shows the current density–voltage (J–V) curves of the PSCs with the precursor−$MAPbI_3$ film, LPI−$MAPbI_3$ film, and $MAPbI_3$–PMMA film, respectively. The precursor−$MAPbI_3$ device shows an open circuit voltage (V_{oc}) of 0.97 V, a short circuit current density (J_{sc}) of 18.9 mA cm^{-2}, a fill factor (FF) of 0.66, and a conversion efficiency of 12.16%. The PSC using LPI−$MAPbI_3$ perovskite film shows a V_{oc} of 1.07 V, J_{sc} of 20.05 mA cm^{-2}, and FF of 0.75, corresponding to a conversion efficiency of 16.13%. In comparison with the precursor–$MAPbI_3$ PSC, all the photovoltaic parameters were improved, especially the V_{oc}, which increased by 0.1 V, probably attributed to the reduction of charge carrier recombination. For the $MAPbI_3$−PMMA, the PSC exhibits a further increased V_{oc} of 1.14 V, with a J_{sc} of 20.01 mA cm^{-2}, and a FF of 0.72, resulting in a conversion efficiency of 16.32%. The V_{oc} of solar cell is typically affected by the shunt resistance, which is associated with charge carrier recombination, mostly determined by the trap-state density of the perovskite light absorber. As discussed above, the assembled PMMA reduces the trap-state density by electronically compensating the I^- vacancy along the boundary, resulting in the V_{oc} improvement for the PSC of $MAPbI_3$−PMMA.

It is worth noting that the PSCs with and without PMMA complexation show comparable photovoltaic performance. The introduction of PMMA by SA complexation did not decrease the photovoltaic performance, which is due to the lowest possible dimensions (monolayer) of PMMA at the boundary of perovskite grain that has a negligible effect on the charge carrier transfer. Figure 3b shows the steady photovoltaic performance and forward–backward scan of J–V curve for the $MAPbI_3$−PMMA cell. The steady state current density was measured at a fixed voltage of 0.89 V, exhibiting magnitude of 17.4 mA cm^{-2}, which corresponds to an efficiency of 15.49%. The efficiency obtained from backward scan J–V curve is 16.32%, while forward scan efficiency is 15.52%. The slight decrease in efficiency obtained from forward scan J–V indicates reduced hysteresis for the PSC. The stability of $MAPbI_3$−PMMA based device was evaluated by measuring the photovoltaic performance versus time, as shown in Figure 3c. The PSC was stored in ambient air (ca. 50% relative humidity) without any encapsulation. During the first 33 days of storage in ambient air, the PSC continued to exhibit 95% of initial efficiency. Sequentially, we increased the humidity and stored the device in a closed chamber with 70% relative humidity. Under these harsh conditions, the device continued to work even on the 50th day with 91% of initial efficiency.

The Complexation of PMMA With $CH_3NH_3PbI_3$: Attenuated total reflectance Fourier-transform infrared (ATR-FTIR) spectroscopy was used to probe the interaction between $MAPbI_3$ and PMMA. The infrared spectrum of CH_3NH_3I (MAI), displayed in **Figure 4**a, demonstrates a significant shift in the NH_3^+ bending mode from 1490 to 1485 cm^{-1} upon complexation with PMMA (MAI−PMMA). Additionally, vibrations assigned to the C−N stretching mode at 991 cm^{-1} and the CH_3 bending mode at 1406 cm^{-1} shift to 989 and 1404 cm^{-1}, respectively.[29,30] PMMA is a well-known Lewis base-type polymer, in which the carbonyl oxygen (C=O) of PMMA serves as an electron pair donor.

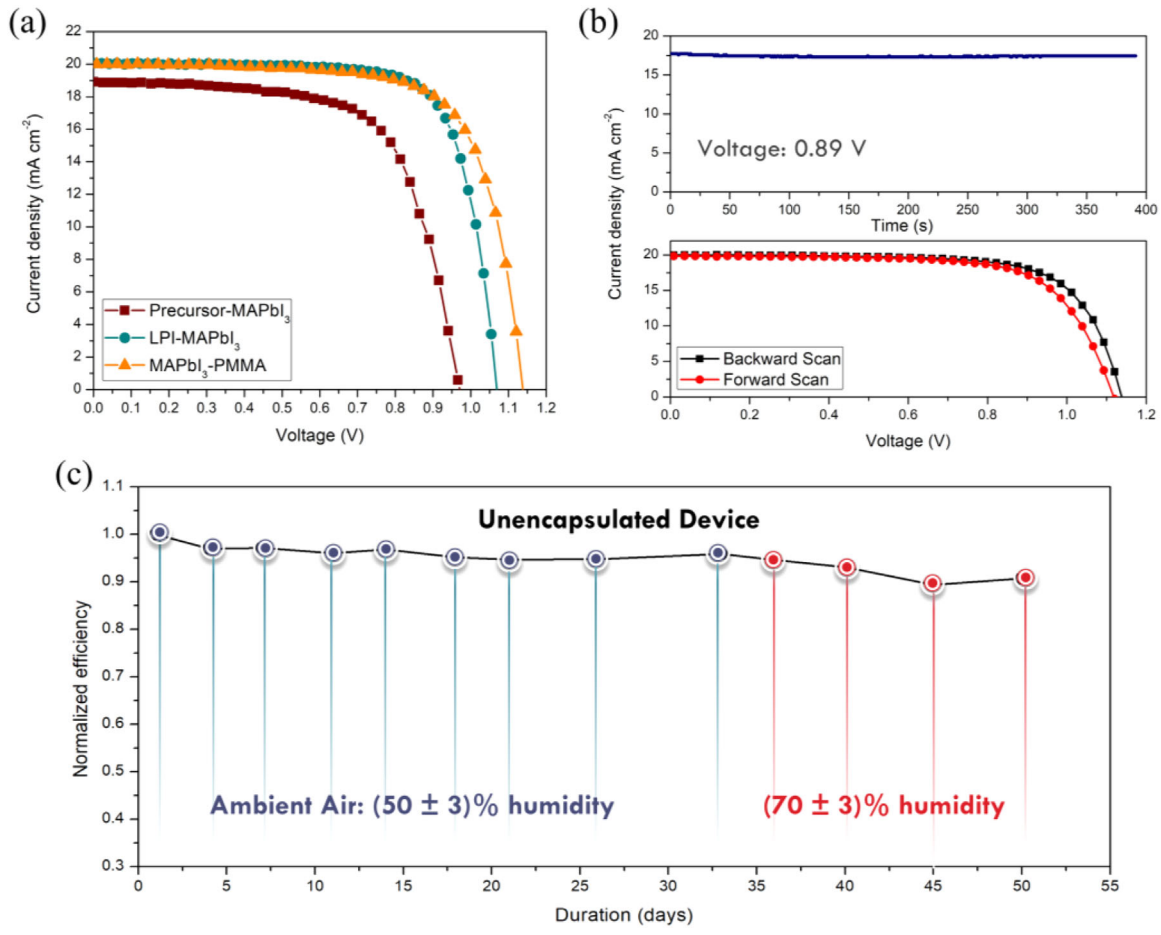

Figure 3. Photovoltaic performance and long-term stability of PSCs. a) Current density–voltage (J–V) curves of the precursor–$MAPbI_3$ device, LPI–$MAPbI_3$ device, and $MAPbI_3$–PMMA device under 1 sun illumination. b) Steady photovoltaic performance and forward–backward scan J–V curve of $MAPbI_3$–PMMA cell. c) The conversion efficiency of $MAPbI_3$–PMMA cell versus time. The device was stored in ambient air (ca. 50% relative humidity) for first 33 days and then stored in 70% humid air until the 50th day.

Decreased vibrational energies in the IR spectrum of MAI–PMMA are consistent with hydrogen bond formation between the C=O of PMMA and NH_3^+ in MAI (O–H), as illustrated in Figure 4c. In order to confirm the interaction between PMMA and MA^+, we fabricated MAI and MAI–PMMA films and stored them in ambient air for 1 day. The MAI film exhibited no obvious physical changes, while the MAI–PMMA film turned yellow (Figure S5a, Supporting Information). UV–vis absorption spectroscopy (Figure S5b, Supporting Information) shows that the MAI film does not absorb ultraviolet (UV) or visible light, but the MAI–PMMA film absorbs strongly around 378 nm, which is attributed to the formation of I_3^-.[31] The change in the light absorption by the MAI–PMMA film is consistent with MA^+ coordinating with PMMA and releasing I^- to be freely dispersed in the matrix. Thereafter, the free I^- can react with O_2 and H_2O in the air, forming I_3^- (Figure S5c, Supporting Information). This result is a further evidence for the complexation between PMMA and MA^+.

In the case of $MAPbI_3$, the chemical complexation is more complicated because the δ^- O in PMMA can interact with both MA^+ and Pb^{2+}.[32] The IR spectra of PMMA, MAI–PMMA, and $MAPbI_3$–PMMA (Figure 4b) show that the C=O stretch in PMMA, located at 1721 cm^{-1}, shifts to 1726 cm^{-1} in both $MAPbI_3$–PMMA and MAI–PMMA, which suggests that the complexation between PMMA and $MAPbI_3$ is analogous to that of PMMA and MAI. In the case of 2D layered perovskite intermediates, the MA^+ ions exposed at the layer surface, favor the interaction between the permanent dipole moment in MA^+ and the polar C=O bond in PMMA. $MAPbI_3$ perovskite consists of MA^+ cations and PbI_3^- anions arranged in an octahedron. Compared with PbI_3^-, MA^+ has a dipole moment that promotes water absorption through hydrogen bonding.[33] The complexation of perovskite with PMMA leads to a monolayer of PMMA anchored between perovskite grains, effectively resembling core-shell morphology. PMMA coating is expected to improve the long-term stability of the perovskite light absorber by isolating MA^+ cations from water molecules in the air, illustrated in Figure 4d. To investigate the hydrophobic effect of PMMA complexation, we measured the water contact angle of $MAPbI_3$, PMMA, and $MAPbI_3$–PMMA films. Contact angles for the three films are 39.1°, 56.9°, and 65.1°, respectively (Figure 4e). Surprisingly, the contact angle for $MAPbI_3$–PMMA is even

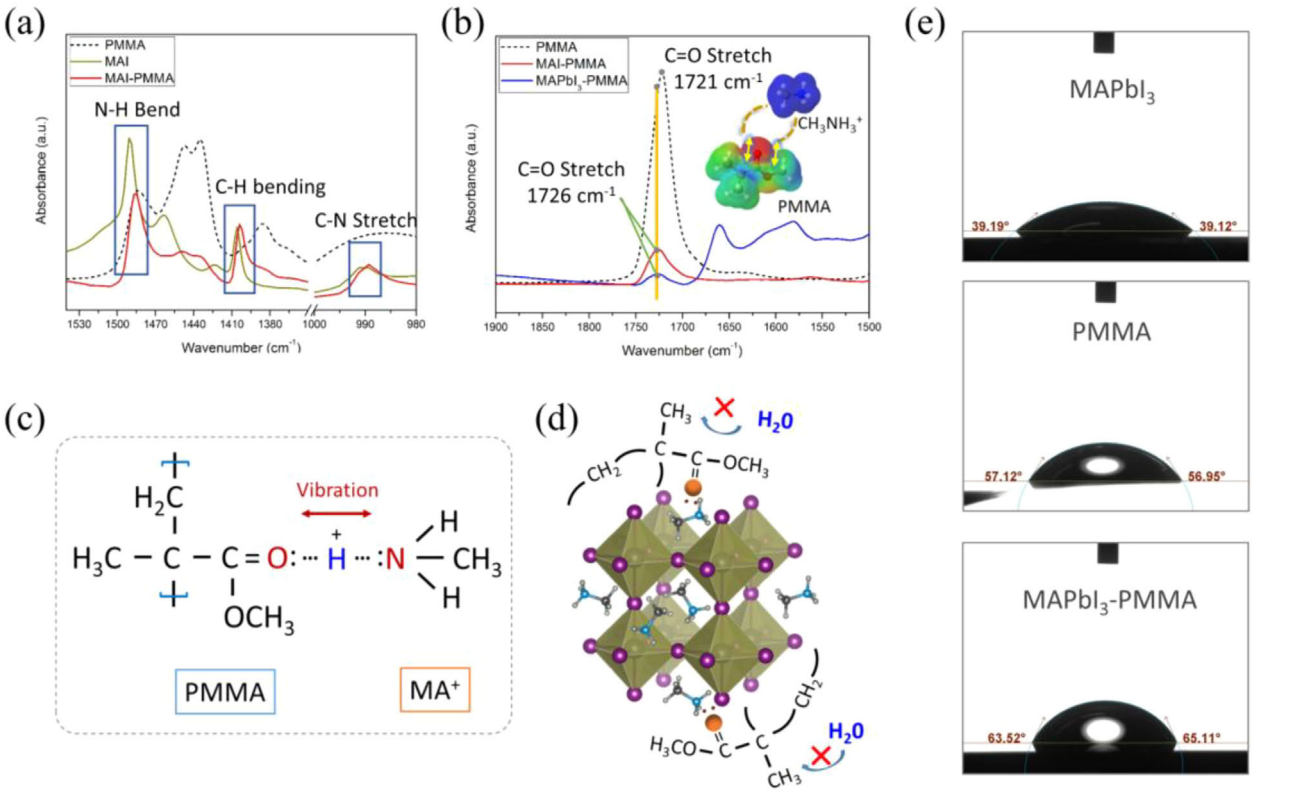

Figure 4. The complexation of $MAPbI_3$ perovskite with PMMA. ATR-FTIR of PMMA, MAI, and MAI−PMMA in the regions from a) 1350–1550 cm^{-1}, 980–1000 cm^{-1}, and b) 1500–1900 cm^{-1}. c) Illustration of the complexation of PMMA with MA^+. d) Schematic illustration of water isolation by PMMA coating on the outer layer of perovskite grains. e) Water contact angle of the $MAPbI_3$ film, PMMA film, and $MAPbI_3$−PMMA film.

greater than that of pristine PMMA. This phenomenon is consistent with O—H hydrogen bond formation between PMMA and $MAPbI_3$, which turns the $-CH_3$ methyl groups of PMMA outward, making the PMMA coating more hydrophobic than pristine PMMA.

Trap Passivation and Carrier Transport: Methods for achieving passivation of electronic defects is critical toward the advancement of thin film solar cells. Prior researchers have employed a thin passivation layer on top of perovskite layer to reduce the surface trap density.[34–36] Here, in the case of $MAPbI_3$−PMMA film, the passivation is supposed to be implemented by the complexation of PMMA along the perovskite grain boundary. To verify the passivation effect, we prepared three samples: pristine perovskite film ($MAPbI_3$), perovskite capped with PMMA layer ($MAPbI_3$+PMMA), and perovskite complexed with PMMA via SA process ($MAPbI_3$−PMMA), respectively. **Figure 5**a shows the steady–state photoluminescence (PL) and absorption spectra of these three films. All of them exhibit identical absorption spectra with cut-off wavelength at 790 nm, corresponding to a band gap of 1.57 eV. However, the PL spectrum differs significantly. Due to the surface trap passivation, the PL intensity of PMMA capped perovskite is higher than that of the pristine perovskite. For the SA $MAPbI_3$−PMMA film, the PL emission intensity is increased even further, which is around three-fold stronger than the pristine perovskite analogue. As mentioned above, the lone pair electrons on C═O in PMMA can electronically passivate the traps that impede the radiative electron-hole recombination by compensating the uncoordinated I^-. The capped PMMA can only reduce the electronic traps at the film surface, whereas the SA PMMA is coated on the boundary of the perovskite grains, which substantially reduces the localized traps along the grain boundary. Figure 5e–g show the PL mapping of the three films with scanning dimension of $40 \times 40\ \mu m^2$. It clearly shows that the entire area becomes brighter in a sequence of $MAPbI_3$, $MAPbI_3$+PMMA, and $MAPbI_3$−PMMA, indicating the smallest trap density for the $MAPbI_3$−PMMA film synthesized by the SA process. Figure 5b compares the XPS between $MAPbI_3$ and $MAPbI_3$−PMMA in the Pb 4f region. The peaks at 138.0 and 142.8 eV correspond to Pb 4f7/2 and Pb 4f5/2 in PbI_3. For the $MAPbI_3^-$ sample, there are another two small peaks located at 136.4 and 141.3 eV, which belong to metallic Pb, while in $MAPbI_3$−PMMA, the peaks for metallic Pb were completely reduced. The presence of metallic Pb is associated with the iodide vacancy in perovskite, which acts as the charge carrier trap sites.[37,38] The elimination of metallic Pb in $MAPbI_3$−PMMA provides further evidence of trap passivation upon the complexation of PMMA with the $MAPbI_3$ perovskite.

To explore the hot-carrier kinetics for the perovskite films, we measured the time-resolved differential reflectivity (TRDR). The pump/probe pulses were tuned at 400 and 800 nm, respectively, and the pulses had a duration of 100 fs. The pump power of 0.3 mW corresponds to a laser fluence of 1 mJ cm^{-2} and was found to result in photo-induced carrier density on the order of

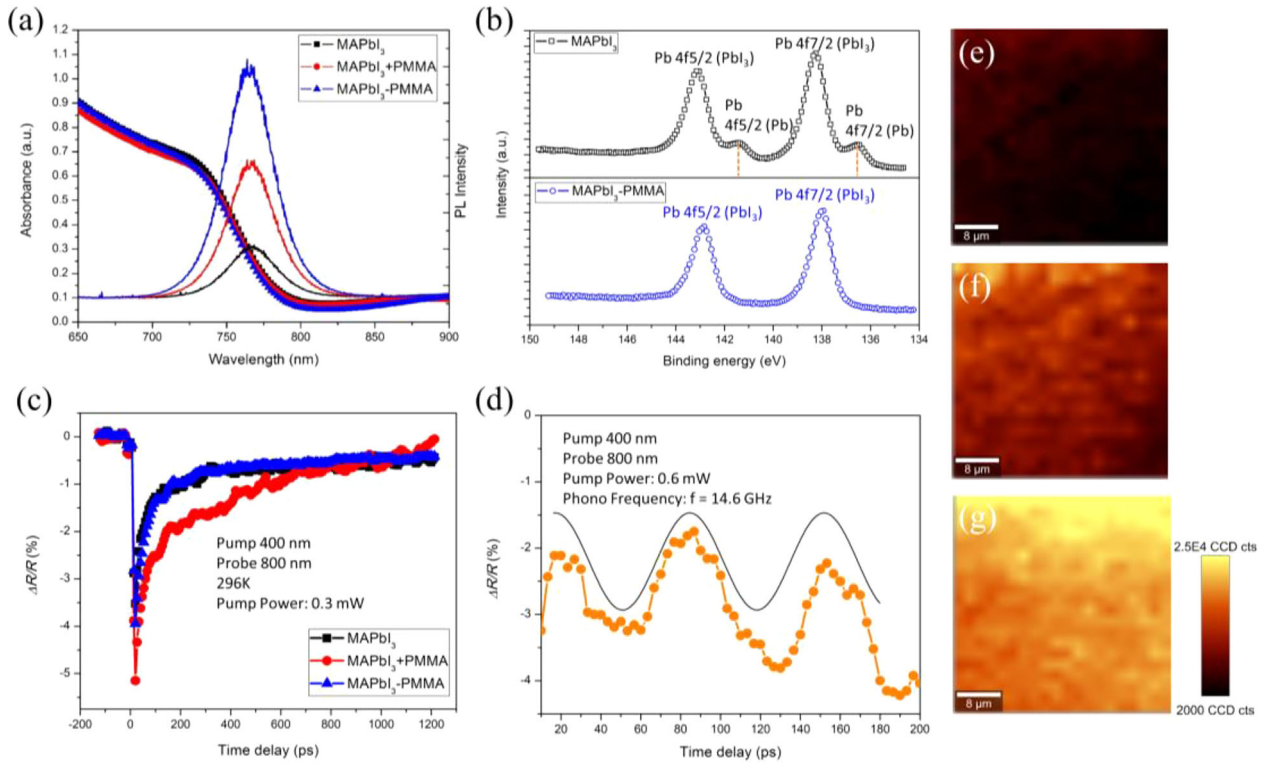

Figure 5. PL and TRDR spectra of perovskite films. a) Steady-state photoluminescence and absorption spectra of $MAPbI_3$ film, $MAPbI_3$+PMMA film, and $MAPbI_3$−PMMA film. b) XPS of $MAPbI_3$ film and $MAPbI_3$−PMMA film in the Pb 4f region. c) TRDR of $MAPbI_3$ film, $MAPbI_3$+PMMA film, and $MAPbI_3$−PMMA film as a function of time delay. d) Close up of the CP oscillations from the perovskite film, in which the fit is shifted for clarity and is corresponding to a phonon frequency of 14.6 GHz. XPS mapping ($40 \times 40\ \mu m^2$) of e) $MAPbI_3$ film, f) $MAPbI_3$+PMMA film, and g) $MAPbI_3$−PMMA film.

$10^{18}\ cm^{-3}$. The relaxations of the photoinduced carriers in the perovskite films can be modeled by 3 time constants, τ_1, τ_2, and τ_3, where τ_1 is attributed to the initial carrier cooling, τ_2 to the relaxation of hot electrons toward the bottom of the conduction band (τ_1 and τ_2 were extracted from a double exponential fit), and τ_3 is the recombination timescale. After the hot electrons are created, the lattice temperature rises, and subsequently the number of longitudinal optical (LO) phonons increases. In the regime of large electron densities, due to screening effects and hot phonons, the photo-excited electrons experience a significant reduction in their energy loss rate through the emissions of LO phonons. The timescale of hot carrier cooling is associated with the carrier transport. The carrier mobility is typically reduced by the internal phonon scattering, which accordingly accelerates the carrier cooling.[39] As shown in Figure 5c, the cooling time τ_1 of the pristine perovskite is 23.6 ps, the PMMA capped one is 27.7 ps, while for the SA PMMA film the cooling time is increased to 34.5 ps. The results indicate that the carrier transport in perovskite is not impeded by the PMMA present on the perovskite grain boundary. Conversely, the transport property is improved. The time scale associated with the carrier cooling toward the conduction band (τ_2) is much longer for the sample capped with PMMA, which might be ascribed to the pump/probe depth at the interface between PMMA and perovskite layer. The carrier recombination (τ_3) remains the same for all three samples (longer than 1.2 ns). In addition to creating non-equilibrium electron-hole pairs, laser pulses can trigger oscillations in the optical properties due to coherent phonons (CP).[40] The CP then modulates the refractive index, which modulates the optical reflectivity of the sample, and can be measured by probe pulses. We observed CP oscillations, with the same period, in all three samples. In Figure 5d, we present an example of the CP oscillations when the pump power was increased. The fit to CP is corresponding to a phonon frequency of 14.6 ± 1.5 GHz, similar to the 12 GHz frequency observed by Mante et al. in single crystal of $MAPbI_3$.[41]

In summary, we have developed a self-assembly process for fabrication of a highly stable $MAPbI_3$ perovskite layer. The hydrophobic polymer PMMA was introduced into the 2D layered perovskite intermediates. This complexation of PMMA with layered perovskites enables a monolayer of PMMA coated on the perovskite grain boundary after the SA process. The anchored PMMA polymer chain effectively blocks water molecules and improves the stability against moisture, light, and oxygen. In addition, the complexation of PMMA is found to reduce trap density along the grain boundary, resulting in V_{oc} improvement of PSC. The PSC shows a conversion efficiency of 16.32% and excellent long-term stability under high humidity environment. This research is providing an easy route to fabricate highly stable PSC without sacrificing photovoltaic performance. Additionally, this approach is applicable with some other more hydrophobic polymers and perovskites, where further improvement in long-term stability could be expected.

Experimental Section

Materials: Methylamine solution (33 wt.% in absolute ethanol), PbI_2, CH_3NH_3I (MAI), acetonitrile (ACN), γ-butyrolactone (GBL), dimethylsulfoxide (DMSO), N,N-dimethylformamide (DMF), toluene, chlorobenzene, diethyl ether, titanium isopropoxide (TTIP), α-terpineol, ethanol were from Sigma–Aldrich. Spiro-OMeTAD was purchased from Luminescence Technology Corp. TiO_2 paste (18NR-T) was acquired from Dyesol. Fluorine-doped tin oxide (FTO) glass was purchased from Nippon Sheet Glass.

Synthesis of $MAPbI_3$ Single Crystals: PbI_2 and MAI (molar ratio 1:1) were dissolved in GBL and stirred at 80 °C for 2 h to form a 1.2 M solution. The solution was filtered into a vial and placed into an oil bath at 110 °C for several hours until black crystals precipitated at the bottom of the vial. Next, the top solvent in the vial was removed and the black crystals were washed with diethyl ether and dried three times.

Synthesis of $MAPbI_3$ ACN Solution: A measured amount of $MAPbI_3$ crystals was placed in a vial which was then sealed into a bottle containing methylamine solution and kept idle overnight. Methylamine gas in the bottle diffused into the vial and reacted with $MAPbI_3$ crystals resulting in liquid perovskite intermediate. The perovskite intermediate was dissolved in ACN to form a 1 M $MAPbI_3$ ACN solution. For $MAPbI_3$−PMMA, PMMA was first dissolved in ACN with a concentration of 9 mg mL^{-1}, then PMMA−ACN solution was used for dissolving perovskite intermediates to form a 1 M solution.

Device Fabrication: FTO glasses were subsequently cleaned with deionized water, acetone, and ethanol and then dried using nitrogen gas. The compact TiO_2 layer was spin-coated on cleaned FTO substrate at 2000 rpm for 20 s using a mildly acidic titanium isopropoxide solution and then heated at 150 °C for 10 min. Mesoporous TiO_2 paste was prepared by diluting TiO_2 paste (18NR-T) in α-terpineol and ethanol (TiO_2: α-terpineol: ethanol = 1:3:1.5 wt.%). After cooling to room temperature, the as-prepared mesoporous TiO_2 paste was spin-coated on the compact TiO_2 layer at 6000 rpm for 30 s, which was then annealed at 500 °C for 1 h. For $MAPbI_3$ layer prepared from 2D layered perovskite intermediates, the $MAPbI_3$ ACN solution with and without PMMA was spin-coated on the TiO_2 layer at 4000 rpm for 20 s and then annealed at 100 °C for 10 min. For the synthesis of precursor−$MAPbI_3$ film, PbI_2 and MAI (molar ratio 1:1) were dissolved in GBL and DMSO (volume ratio 7:3) and stirred at 70 °C to form a 1.2 M solution. After complete dissolution, the solution was filtered and then spin-coated on the TiO_2 layer at 4000 rpm for 20 s with toluene as anti-solvent, followed by annealing at 100 °C for 10 min. Next, the spiro-OMeTAD solution was spin-coated on perovskite layer at 4000 rpm for 20 s. At last, 80 nm of gold was evaporated on top of spiro-OMeTAD as electrode over an active area of 0.096 cm^2.

Characterization: Attenuated total reflectance Fourier-transform infrared spectroscopy (ATR-FTIR) was measured using a Varian 670-IR spectrometer.X-ray photoelectron spectroscopy (XPS) was performed using PHI VersProbe III. Spectra were acquired using monochromatic Al K-alpha X-ray source (1486.6 eV) at 100 W over 1400 × 100 μm^2 area at 45° angle. XPS mapping was acquired over 300 × 300 μm^2 area with 15 μm 2.5 W^{-1} X-ray beam. Conductive atomic force microscopy (c-AFM) was measured by Park XE7 atomic force microscope with the external I-AFM model. Measurements were carried out at bias voltage of 2 V and scan rate of 0.5 Hz. X-ray diffraction (XRD) analyses were conducted using Philips Xpert Pro X-ray diffractometer (Almelo, The Netherlands). UV–vis absorption spectra were recorded using U-4100, Hitachi UV–vis spectrophotometer. Steady-state photoluminescence (PL) was conducted using WITec 300 R system with 633 nm excitation. The spectrum was averaged by 100 spectra in a randomly selected area of 40 × 40 μm^2. Time-resolved differential transmission (TRDR) pump/probe was measured by laser source of an amplified Ti: sapphire oscillator with a repetition rate of 1 kHz. The pump/probe pulses were tuned at 400 and 800 nm, respectively, and the pulses had a duration of 100 fs defining the resolution of the measurements. Both beams were focused onto the sample with a spot size of around 150–200 μm for probe pulses, and slightly larger for the pump. The pump/probe ratio of 1000:1, was kept for all the measurements, and the TRDR as a function of the time delay between the pump and probe pulses, using a Si detector, was recorded. Scanning electron microscopy (SEM) images were obtained using scanning electron microscopy (SEM, Quanta 600 FEG, FEI). Cross-sectional HRTEM sample is prepared using a standard focused ion beam lift-out procedure (FEI Helios 600), and sample is mounted on molybdenum support grid. The HRTEM image is measured using JEOL 2100 TEM. *J–V* characteristics of the solar cells were recorded by a Keithley digital source meter (Model 2400) under one sun (AM 1.5 G, 100 mW cm^{-2}) illumination provided by a solar simulator (150 W Sol 2ATM, Oriel).

Supporting Information

Supporting Information is available from the Wiley Online Library or from the author.

Acknowledgements

C.W. acknowledges the financial support from the Institute of Critical Technology and Applied Science (ICTAS). S.P. would like to acknowledge the financial support from Office of Naval Research (I. Perez). Y.Y. was supported through the AMRDEC participation in NSF I/UCRC: Center for Energy Harvesting Materials and Systems (CEHMS). G. A. K acknowledges the supports from: FA9550-16-1-0358 under DURIP2016, AFOSR grant FA9550-14-1-0376, FA9550-17-1-0341, and the Institute of Critical Technology and Applied Science at Virginia Tech. We thank Ya-Peng Yu and Christopher Winkler at Nanoscale Characterization and Fabrication Lab, Virginia Tech for the FIB lift-out and TEM measurement. We thank Dr. Xu Feng and the Surface Analysis Laboratory at Virginia Tech for the XPS analysis. We thank Dr. Weinan Leng and VTSuN Lab at Virginia Tech for the PL measurement.

Conflict of Interest

The authors declare no conflict of interest.

Keywords

hydrophobic polymers, intermediates, perovskite films, self assembly, long-term stability, trap passivation

Received: February 21, 2018
Revised: March 6, 2018
Published online:

[1] M. Gratzel, *Nat. Mater.* **2014**, *13*, 838.
[2] H. J. Snaith, *J. Phys. Chem. Lett.* **2013**, *4*, 3623.
[3] M. A. Green, A. Ho-Baillie, H. J. Snaith, *Nat. Photon.* **2014**, *8*, 506.
[4] H.-S. Kim, C.-R. Lee, J.-H. Im, K.-B. Lee, T. Moehl, A. Marchioro, S.-J. Moon, R. Humphry-Baker, J.-H. Yum, J. E. Moser, M. Grätzel, N.-G. Park, *Sci. Rep.* **2012**, *2*, 591.
[5] Y. Sun, C. Wang, D. Zhao, J. Yu, X. Yin, C. R. Grice, R. A. Awni, N. Shrestha, Y. Yu, L. Guan, R. J. Ellingson, W. Tang, Y. Yan, *Sol. RRL* **2018**, *2*, 1700175.
[6] M. Xie, H. Lu, L. Zhang, J. Wang, Q. Luo, J. Lin, L. Ba, H. Liu, W. Shen, L. Shi, C.-Q. Ma, *Sol. RRL* **2018**, *2*, 1770152.
[7] C. Liang, P. Li, H. Gu, Y. Zhang, F. Li, Y. Song, G. Shao, N. Mathews, G. Xing, *Sol. RRL* **2018**, *2*, 1770150.
[8] A. Kojima, K. Teshima, Y. Shirai, T. Miyasaka, *J. Am. Chem. Soc.* **2009**, *131*, 6050.

[9] S. D. Stranks, G. E. Eperon, G. Grancini, C. Menelaou, M. J. P. Alcocer, T. Leijtens, L. M. Herz, A. Petrozza, H. J. Snaith, *Science* **2014**, *342*, 341.
[10] J. Wang, F. Di Giacomo, J. Brüls, H. Gorter, I. Katsouras, P. Groen, R. A. J. Janssen, R. Andriessen, Y. Galagan, *Sol. RRL* **2017**, *1*, 1700091.
[11] F. Matteocci, L. Cinà, E. Lamanna, S. Cacovich, G. Divitini, P. A. Midgley, C. Ducati, A. Di Carlo, *Nano Energy* **2016**, *30*, 162.
[12] H. C. Weerasinghe, Y. Dkhissi, A. D. Scully, R. A. Caruso, Y. B. Cheng, *Nano Energy* **2015**, *18*, 118.
[13] F. Bella, G. Griffini, J.-P. Correa-Baena, G. Saracco, M. Gratzel, A. Hagfeldt, S. Turri, C. Gerbaldi, *Science* **2016**, *354*, 203.
[14] Y. Bai, Q. Dong, Y. Shao, Y. Deng, Q. Wang, L. Shen, D. Wang, W. Wei, J. Huang, *Nat. Commun.* **2016**, *7*, 12806.
[15] Q. Wang, B. Chen, Y. Liu, Y. Deng, Y. Bai, Q. Dong, J. Huang, *Energy Environ. Sci.* **2017**, *10*, 516.
[16] F. Bella, E. D. Ozzello, S. Bianco, R. Bongiovanni, *Chem. Eng. J.* **2013**, *225*, 873.
[17] G. P. Salvador, D. Pugliese, F. Bella, A. Chiappone, A. Sacco, S. Bianco, M. Quaglio, *Electrochim. Acta* **2014**, *146*, 44.
[18] M. Gerosa, A. Sacco, A. Scalia, F. Bella, A. Chiodoni, M. Quaglio, E. Tresso, S. Bianco, *IEEE J. Photovolt.* **2016**, *6*, 498.
[19] P. Tyagi, S.-C. Hua, D. R. Amorim, R. M. Faria, J. Kettle, M. Horie, *Org. Electron.* **2018**, *55*, 146.
[20] F. Wang, A. Shimazaki, F. Yang, K. Kanahashi, K. Matsuki, Y. Miyauchi, T. Takenobu, A. Wakamiya, Y. Murata, K. Matsuda, *J. Phys. Chem. C* **2017**, *121*, 1562.
[21] X. Wen, J. Wu, M. Ye, D. Gao, C. Lin, *Chem. Commun.* **2016**, *52*, 11355.
[22] Q. Dong, Y. Fang, Y. Shao, P. Mulligan, J. Qiu, L. Cao, J. Huang, *Science* **2015**, *347*, 967.
[23] D. Shi, V. Adinolfi, R. Comin, M. Yuan, E. Alarousu, A. Buin, Y. Chen, S. Hoogland, A. Rothenberger, K. Katsiev, Y. Losovyj, X. Zhang, P. A. Dowben, O. F. Mohammed, E. H. Sargent, O. M. Bakr, *Science* **2015**, *347*, 519.
[24] B. Saparov, D. B. Mitzi, *Chem. Rev.* **2016**, *116*, 4558.
[25] C. Wu, H. Li, Y. Yan, B. Chi, J. Pu, J. Li, M. Sanghadasa, S. Priya, *Nano Energy* **2017**, *36*, 295.
[26] N. Ahn, K. Kwak, M. S. Jang, H. Yoon, B. Y. Lee, J.-K. Lee, P. V. Pikhitsa, J. Byun, M. Choi, *Nat. Commun.* **2016**, *7*, 13422.
[27] D. Bryant, N. Aristidou, S. Pont, I. Sanchez-Molina, T. Chotchunangatchaval, S. Wheeler, J. R. Durrant, S. A. Haque, *Energy Environ. Sci.* **2016**, *9*, 1655.
[28] N. Aristidou, C. Eames, I. Sanchez-Molina, X. Bu, J. Kosco, M. S. Islam, S. A. Haque, *Nat. Commun.* **2017**, *8*, 15218.
[29] A. Cabana, C. Sandorfy, *Spectrochim. Acta* **1962**, *18*, 843.
[30] J. B. Patel, R. L. Milot, A. D. Wright, L. M. Herz, M. B. Johnston, *J. Phys. Chem. Lett.* **2016**, *7*, 96.
[31] J. M. Gardner, M. Abrahamsson, B. H. Farnum, G. J. Meyer, *J. Am. Chem. Soc.* **2009**, *131*, 16206.
[32] N. Ahn, D.-Y. Son, I.-H. Jang, S. M. Kang, M. Choi, N.-G. Park, *J. Am. Chem. Soc.* **2015**, *137*, 8696.
[33] Z. Zhu, V. G. Hadjiev, Y. Rong, R. Guo, B. Cao, Z. Tang, F. Qin, Y. Li, Y. Wang, F. Hao, S. Venkatesan, W. Li, S. Baldelli, A. M. Guloy, H. Fang, Y. Hu, Y. Yao, Z. Wang, J. Bao, *Chem. Mater.* **2016**, *28*, 7385.
[34] F. Wang, W. Geng, Y. Zhou, H. H. Fang, C. J. Tong, M. A. Loi, L. M. Liu, N. Zhao, *Adv. Mater.* **2016**, *28*, 9986.
[35] Y. Lin, L. Shen, J. Dai, Y. Deng, Y. Wu, Y. Bai, X. Zheng, J. Wang, Y. Fang, H. Wei, W. Ma, X. C. Zeng, X. Zhan, J. Huang, *Adv. Mater.* **2017**, *29*, 1604545.
[36] N. K. Noel, A. Abate, S. D. Stranks, E. S. Parrott, V. M. Burlakov, A. Goriely, H. J. Snaith, *ACS Nano* **2014**, *8*, 9815.
[37] H. Cho, S.-H. Jeong, M.-H. Park, Y.-H. Kim, C. Wolf, C.-L. Lee, J. H. Heo, A. Sadhanala, N. Myoung, S. Yoo, S. H. Im, R. H. Friend, T.-W. Lee, *Science* **2015**, *350*, 1222.
[38] D. Bi, C. Yi, J. Luo, J.-D. Décoppet, F. Zhang, S. M. Zakeeruddin, X. Li, A. Hagfeldt, M. Grätzel, *Nat. Energy* **2016**, *1*, 16142.
[39] M. B. Price, J. Butkus, T. C. Jellicoe, A. Sadhanala, A. Briane, J. E. Halpert, K. Broch, J. M. Hodgkiss, R. H. Friend, F. Deschler, *Nat. Commun.* **2015**, *6*, 8420.
[40] B. A. Magill, K.-D. Park, Y. Zhou, A. Chopra, D. Maurya, S. Priya, M. Raschke, A. Belyanin, C. J. Stanton, G. A. Khodaparast, *Energy Harvest Syst.* **2016**, *3*, 229.
[41] P.-A. Mante, C. C. Stoumpos, M. G. Kanatzidis, A. Yartsev, *Nat. Commun.* **2017**, *8*, 14398.